


 Cite this: *RSC Adv.*, 2025, **15**, 41497

Sustainable ZnO synthesis from skim latex serum wastewater for efficient dye degradation and enhanced rubber vulcanization

 Sopinya Nithakorn,^a Thanthapatra Bunchuay^{bc} and Preeyanuch Junkong  ^{id} ^{*a}

This study presents a sustainable approach for synthesizing zinc oxide (ZnO) using skim latex serum, a wastewater from concentrated latex manufacturing. Utilizing biomolecules in the serum as capping and stabilizing agents, ZnO yield increases 25-fold through a precipitation method. The resulting ZnO features a unique flower-like morphology, observed by field-emission scanning electron microscopy, with particle size controllable by adjusting serum content. Higher serum levels result in smaller and more uniform ZnO structures, as the serum enhances nucleation while simultaneously impeding particle growth. For the first time, a reaction mechanism is proposed for ZnO synthesis from skim latex serum wastewater, identifying the plausible pathways through a serum-based precipitation method, and elucidating the role of serum constituents and NaOH in morphology control. This flower-like ZnO shows effective photocatalytic activity, degrading dyes through the pseudo-zero-order kinetic process, and demonstrates recyclability. Furthermore, it functions as an activator in rubber vulcanization. Rubber vulcanizates prepared with the synthesized ZnO show curing and mechanical properties comparable to those prepared with commercial ZnO. Fourier-transform infrared spectroscopy confirms the formation of zinc-stearate with monodentate coordination upon reaction with stearic acid at 144 °C, consistent with the behavior of commercial ZnO. This dual functionality as both a photocatalyst and a vulcanization activator underscores the potential of flower-like ZnO as an alternative for conventional ZnO. The process contributes to Sustainable Development Goal 6 by valorizing industrial wastewater, and exemplifying a circular economy. Overall, this work integrates environmental stewardship with high-performance applications in environmental remediation and rubber technology.

 Received 23rd August 2025
 Accepted 21st October 2025

DOI: 10.1039/d5ra06278k

rsc.li/rsc-advances

1 Introduction

Among the variety of metal oxide materials, zinc oxide (ZnO) captures the attention of researchers owing to its unique properties, which have led to its widespread utilization across various applications. With a large band gap and high binding energy, ZnO plays a crucial role in optoelectronic devices,¹ sensors,² and photocatalysts.^{3–5} Additionally, its remarkable biocompatibility and low toxicity make it a preferred choice for drug transport, anti-cancer, anti-diabetic, and other biomedical applications.^{4–8} Moreover, ZnO finds utility in agriculture owing to its antinematode and anti-fungal and serves as an additive in plastic and rubber as well as a UV protection agent.^{9–12} The synthesis of ZnO can be accomplished through various approaches, such as the sol-gel method,¹³ hydrothermal

method,¹⁴ precipitation,¹⁵ ultrasonic irradiation,¹⁶ thermal evaporation.¹⁷ In addition to the traditional synthesis routes, the green synthesis has emerged as a noteworthy approach in research due to its cost-effectiveness, simplicity, efficiency, and eco-friendliness.¹⁸ Typically, the green synthesis entails utilizing natural resources, such as plant extracts, microorganisms, and biomolecules.¹⁹ Among the available green methods, the utilization of plant extracts is a rather simple and easy process to produce the ZnO particles at a large scale. This is mainly due to the high content of bioactive compounds in plant extracts, which are used as *in situ* reducing and stabilizing agents for ZnO formation.²⁰ In recent studies, various plant extracts have been utilized for the green synthesis of ZnO particles and demonstrated their potential in different applications.^{21–37} Particularly, several researchers have pointed out the practice of photocatalytic ZnO-based processes in the removal of dyes from wastewater.^{24,36,37} This is mainly due to its ability to completely mineralize pollutants by forming electron-hole pairs under ultraviolet or visible light radiation. Manojkumar *et al.* synthesized ZnO using *Brassica oleracea* var. *botrytis* leaf extracts, confirming the presence of plant extract functional groups as reducing agents by Fourier-transform

^aDepartment of Chemistry, Faculty of Science, Mahidol University, Ratchathewi, Bangkok 10400, Thailand. E-mail: preeyanuch.jun@mahidol.ac.th

^bDepartment of Chemistry, Center of Excellence for Innovation in Chemistry (PERCH-CIC), Faculty of Science, Mahidol University, Bangkok 10400, Thailand

^cCenter of Sustainable Energy and Green Materials, Faculty of Science, Mahidol University, Salaya, Phutthamonthon, Nakhon Pathom 73170, Thailand





infrared spectroscopy. These nanoparticles displayed capabilities in dye degradation, including antimicrobial and larvicidal activities.³⁶ Recently, para rubber leaf extract was employed as a capping agent, and para wood ash extract served as a natural alkaline source for ZnO synthesis. The X-ray diffraction (XRD) results confirmed the formation of the hexagonal wurtzite structure, while scanning electron microscopy revealed predominantly spherical particles with an average size of 91.60 nm. These biosynthesized ZnO particles demonstrated promising properties for environmental applications, such as the photodegradation of organic pollutants and antimicrobial activity.³⁸ Other plant extracts, including those from *Withania coagulans*,²⁹ *Syzygium cumini*,³¹ and *Citrus sinensis*,³² have also been effective in ZnO synthesis. Additionally, latex from *Euphorbia jatropa*,²³ *Euphorbia tirucalli*,^{22,26} *Calotropis procera*,²¹ and milkweed (*Calotropis gigantea* L. R. Br)²⁵ has been used for ZnO synthesis. For instance, *Carica papaya* milk (CPM) latex produced ZnO nanoparticles with different morphologies like hexagonal pyramids and nanoflowers, with promising photocatalytic properties for dye degradation.²⁴ *Brosimum parinarioides* latex also facilitated ZnO synthesis, as confirmed by XRD patterns showing the hexagonal wurtzite structure, and demonstrated effective methylene blue dye degradation under visible light.³⁷ As previously noted, ZnO is widely employed in the rubber industry for manufacturing various rubber products. It is well recognized as an effective vulcanization activator, enhancing the rate of sulfur cross-linking in rubber matrices. It was reported that ZnO nanoparticles synthesized using Aloe vera extract and zinc nitrate (1 : 1 molar ratio) were incorporated into natural rubber (NR). The bioZnO showed sulfur curing efficiency comparable to commercial ZnO.³⁹ Additionally, NR composites containing bioZnO exhibited enhanced mechanical strength and superior thermo-oxidative aging resistance, highlighting its potential as a sustainable alternative in rubber formulations.³⁹ Further studies reported the synthesis of ZnO using *Aloysia citrodora* leaf water extract as both reducing and capping agents in an alkaline environment. When used in styrene-butadiene rubber/natural rubber (SBR/NR) vulcanizates at a reduced loading of 0.5 phr, the green ZnO showed improved curing and mechanical properties compared to commercial ZnO at 5 phr. This enhancement was attributed to the uniform distribution and fine dispersion of ZnO nanoparticles within the rubber matrix.⁴⁰ Moreover, ZnO synthesized using mango (*Mangifera indica*) leaf extract yielded nanoparticles with an average diameter of 65.19 nm, as confirmed by transmission electron microscopy. At 2 phr loading, these ZnO particles achieved an optimal cure time equivalent to that of conventional ZnO at 5 phr, indicating efficient curing performance with reduced additive content.⁴¹

For rubber industries, concentrated latex is an essential intermediate material, serving as the primary raw material for dipped goods, adhesives, foams, and various high-performance rubber products. It is a refined form of NR latex in which dry rubber content (DRC) is typically raised from about 30–35% in field NR latex to 60%, primarily through centrifugation. During this process, skim latex with a DRC of about 3–7% is produced as a significant by-product. When skim latex is destabilized—for

example, through acid coagulation—or when its rubber lumps are washed for use in the manufacture of lower-grade block rubber,^{42,43} the resulting aqueous stream, known as skim latex serum wastewater, is generated. This wastewater is released along with other effluents into a treatment pond. For instance, processing 1000 kilograms of field NR latex into concentrated latex produces approximately 2430 liters of wastewater, with around 580 liters, or 24%, coming from skim latex serum.⁴⁴ The conventional disposal method poses significant environmental challenges. This is because the skim latex serum wastewater predominantly contains water and various biomolecules such as proteins (approximately 3% by weight), lipids (around 0.4% by weight), and carbohydrates/sugars (about 3% by weight), including L-quebrachitol, sucrose, glucose, fructose, raffinose, and pentose,⁴² which can react with microorganisms, resulting in pollutants and foul odors in factories and surrounding areas. However, several studies as mentioned earlier have been reported that these organic substances can act as reducing, capping, and stabilizing agents in the synthesis of ZnO.^{45,46} By exploring the potential of skim latex serum wastewater as a resource for ZnO synthesis, we can reduce wastewater production and mitigate environmental impacts while leveraging its organic components for value-added applications.

In this research, the skim latex serum wastewater was successfully used for the synthesis of ZnO for the first time. The formation mechanism of ZnO synthesized using skim latex serum as capping and stabilizing agents was proposed. Using this sustainable synthesis method, the morphological flower-like shape of ZnO could be controlled. Also, the flower-like ZnO was proven to be a photocatalyst for dye degradation. The efficiency for dye degradation of flower-like ZnO and its recyclability were systematically evaluated. In addition, the functional performance of this ZnO was investigated for its potential use in rubber formulations, particularly its chemical reactivity with stearic acid and other curatives during sulfur vulcanization. The photocatalytic and vulcanization performances of the flower-like ZnO were assessed in comparison with commercial ZnO.

2 Experimental

2.1 Chemical reagents

Skim latex was supplied by Thai Rubber Latex Group PCL, Chonburi, Thailand. Zinc acetate dihydrate ($Zn(CH_3COO)_2 \cdot 2H_2O$; KEMAUS, analytical grade) and zinc nitrate hexahydrate ($Zn(NO_3)_2 \cdot 6H_2O$; KEMAUS, analytical grade) were bought from Molecule Co. Ltd, Bangkok, Thailand. Sodium hydroxide ($NaOH$; analytical grade) was supplied from S.P.S. Lab Co. Ltd, Nonthaburi, Thailand. Methylene blue (KEMAUS, laboratory grade) was obtained from TTK Science Co. Ltd, Bangkok, Thailand. Isoprene rubber (IR; Nipol IR2200GA) was received from Zeon Corporation, Japan. Stearic acid (StH; PALMAC 1500) was obtained from IOI Acidchem Sdn. Bhd., Malaysia. Commercial ZnO (white seal) was sourced from Thai-Lysaght Co. Ltd, Thailand. *N*-(1,3-Dimethylbutyl)-*N*'-phenyl-*p*-phenylenediamine (CBS; Monflex) was provided by Northeast Auxiliary Chemical Industry Co. Ltd, China. Sulfur (S_8 ; commercial grade)

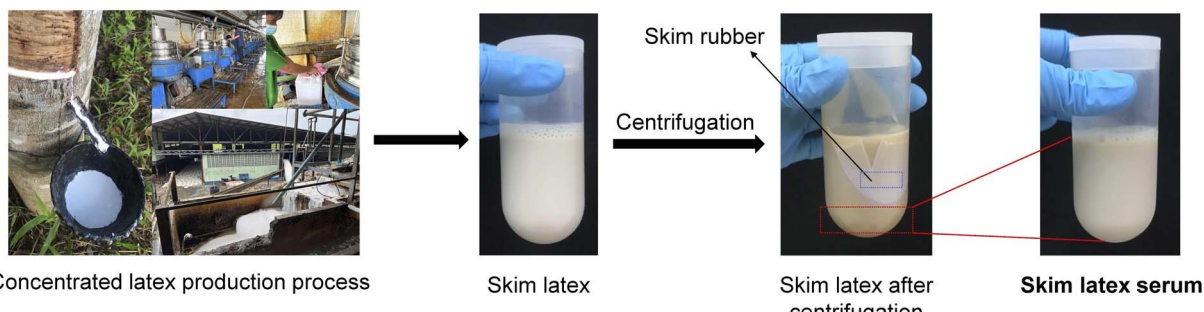


Fig. 1 Extraction of skim latex serum from the skim latex by the centrifugation method.

was purchased from Thai Siam Chemicals Public Co. Ltd, Thailand. Toluene (commercial grade) was obtained from RCI Labscan Co. Ltd, Thailand.

2.2 Extraction of skim latex serum wastewater

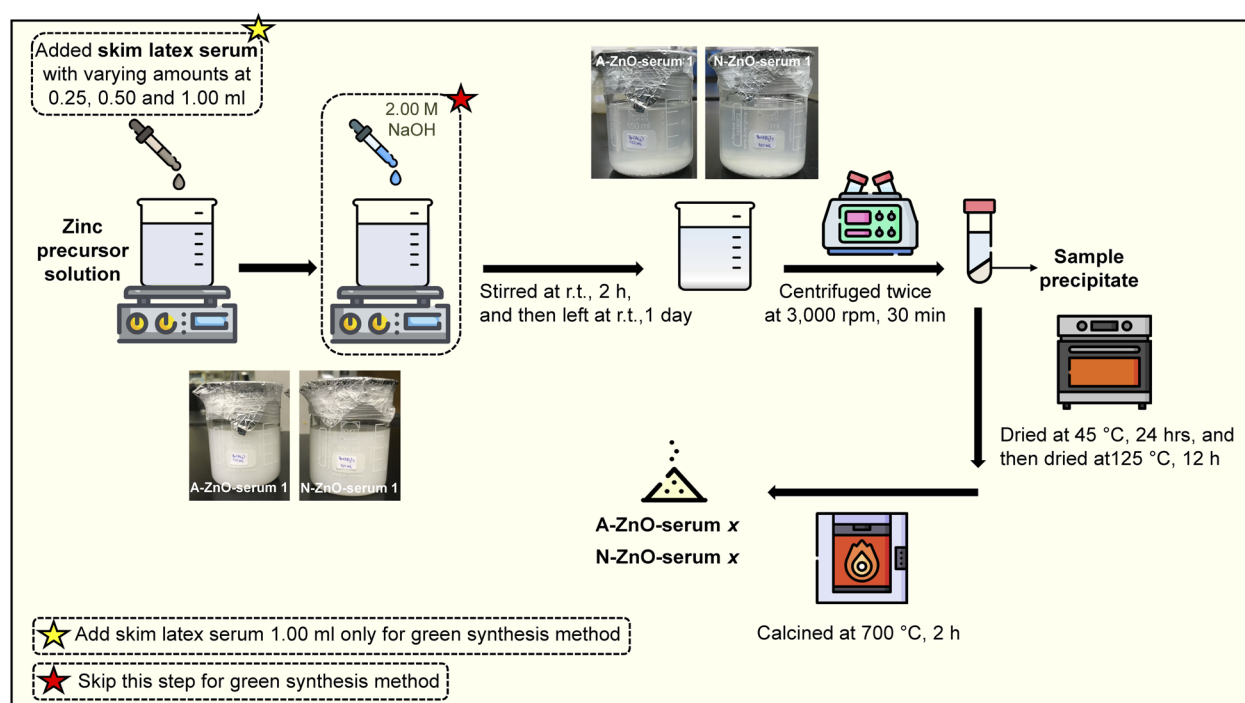
The skim latex serum wastewater in this study was separated from the skim latex by the centrifugation method. The skim latex was centrifuged at 12 000 rpm, for 30 min. The centrifugation was repeated twice. The skim rubber accumulated and floated up to the top layer, and then the skim latex serum at the lower layer was separated and kept in the refrigerator (Fig. 1).

2.3 Synthesis of ZnO

2.3.1 Green synthesis. The green synthesis of ZnO using skim latex serum wastewater is illustrated in Scheme 1. In this process, 1 ml of skim latex serum was added into 100 ml of 0.01 M zinc acetate or zinc nitrate solution. The mixture was

continuously stirred at room temperature (r.t.) for 2 h. A cloudy solution containing white precipitates was then obtained and allowed to stand undisturbed for 1 day. These white precipitates were separated by centrifugation at 3000 rpm for 30 min, with the centrifugation process being repeated twice. After that, the white precipitates were dried at 45 °C for 24 h and at 125 °C for 12 h. The dried powder was calcined at 700 °C for 2 h, where a powdery, light yellow product was obtained.

2.3.2 Serum-based precipitation method. The ZnO was synthesized through a serum-based precipitation method, which was adapted from a green synthesis method as shown in Scheme 1. The process employed varying volumes of skim latex serum: 0.00, 0.25, 0.50, and 1.00 ml. Moreover, 2.40 ml of 2.00 M NaOH solution was added dropwise into the mixture before stirring at r.t. for 2 h. Here, the ZnO synthesized from zinc acetate and zinc nitrate through the serum-based precipitation method was abbreviated as A-ZnO-serum x and N-ZnO-serum x , respectively, where x is the amount of skim latex serum added.



Scheme 1 The synthesis of ZnO using skim latex serum wastewater.



Additionally, the code C-ZnO is used for the commercial ZnO. % yield of the synthesized ZnO was calculated using the equation below.

$$\% \text{ yield} = \frac{\text{actual yield}}{\text{theoretical yield}} \times 100 \quad (1)$$

2.4 Characterizations of skim latex serum and ZnO

The nitrogen content (% N) of the frozen-dried skim latex serum was determined using the Kjeldahl method by the nitrogen analyzer (Kjeltec 8400, FOSS). The nitrogen analysis was conducted according to the in-house method based on ISO 1656. The reported % N value represents the average of three measurements. Functional groups of the biomolecules in the skim latex serum and the ZnO were investigated by Fourier-transform infrared spectroscopy (FT-IR; Frontier, PerkinElmer). The FT-IR spectra of the samples were scanned in the range of 4000–400 cm^{-1} (16 scans per time) using single-reflection attenuated total reflectance mode at r.t. with a spectral resolution of 4 cm^{-1} . The crystalline structure of the ZnO was investigated using a powder X-ray diffraction (PXRD) (D2 Phaser, Bruker). The PXRD used monochromatic X-ray with Cu K_α radiation ($\lambda = 1.54184 \text{ \AA}$) and operated at 30 kV/10 mA. A scanning range was $2\theta = 30\text{--}80^\circ$ with a scanning rate of 0.02° per step. The morphologies of the ZnO were observed by field-emission scanning electron microscopy with energy dispersive X-ray spectroscopy (FESEM-EDX; SU-8010, Hitachi). The ZnO powder was scattered on the carbon tape and then coated with Platinum–Palladium (Pt–Pd) before being examined under an FE-SEM. Herein, the average particle size of ZnO was determined from the FE-SEM images using ImageJ software. Specific surface area measurements of ZnO were conducted at 77 K using a gas adsorption analyzer (3Flex, Micromeritics), and the data were evaluated according to the Brunauer–Emmett–Teller (BET) theory.

2.5 Photocatalytic dye degradation

The ZnO sample was added to 1 ppm of methylene blue solution in a ratio of 1 : 1 (mg of ZnO : ml of methylene blue solution).^{47–50} The resulting mixture was stirred at r.t. under dark condition for 2 h to reach a methylene blue adsorption–desorption equilibrium by the ZnO. Then, the ZnO/methylene blue mixture was irradiated under a UV light lamp (254 nm) for different time intervals, *i.e.*, 0, 5, 35, 65, 95, 125, 155, 185 min. The supernatant of the ZnO/methylene blue mixture solution taken at various time intervals after UV irradiation was subjected to a UV-vis spectrophotometer (UV-1800, Shimadzu). The UV-vis spectra of the methylene blue solutions taken at different time intervals were recorded in the range of 500–800 nm. The time-dependent amount of the dye degraded per unit mass of the ZnO (q_t) was calculated using eqn (2).⁵¹

$$q_t = \frac{C_0 - C_t}{m} \times V \quad (2)$$

where C_0 and C_t are the concentration of methylene blue solution (mg L^{-1}) at 0 and t min, respectively. V is the volume (L) of a solution, and m is the mass (g) of the ZnO.

To evaluate the recyclability of ZnO in photocatalytic dye degradation, the ZnO samples were subjected to the photocatalytic degradation experiment for methylene blue dye three consecutive times. Following each 185 min photocatalytic experiment, the ZnO samples were rinsed three times with 20.00 ml of distilled water, with each rinsing session involving 10 min of stirring. Subsequently, the rinsed ZnO samples were dried overnight at 80 °C before being reused in the next cycle of photocatalytic degradation. In parallel, the supernatant from each ZnO/methylene blue mixture solution was subjected to a UV-vis spectrophotometer (UV-1800, Shimadzu), and the dye degradation efficiency of each cycle was calculated using eqn (3).³

$$\text{Degradation efficiency (\%)} = \frac{C_i - C_f}{C_i} \times 100 \quad (3)$$

where C_i and C_f are the initial and final concentrations of methylene blue solution (mg L^{-1}), respectively. The reported average dye degradation efficiency of each cycle was determined by four experiments.

2.6 Activator for rubber vulcanization

ZnO (using commercial ZnO or A-ZnO-serum 1) of 0.5 phr, StH of 2 phr, CBS of 1 phr and S₈ of 1.5 phr were mixed with IR on a two-roll mill (W100T; COLLIN Lab & Pilot Solutions GmbH) at r.t. Each compound was subsequently molded into a sheet of 1 mm thickness by using a compression molding machine (G30H-15-CX; WABASH) at 21 MPa and 144 °C for the respective cure time (t_{c90}). Cure characteristics were determined at 144 °C with a moving die rheometer (MDR; MDR-01; CGM Technology Co. Ltd) in accordance with ISO 6502. The reported values represent the average of three independent measurements. A thermal behavior was analyzed using a differential scanning calorimeter (DSC; Q200-RCS90; TA Instruments). Approximately 7–10 mg of the rubber compounds were encapsulated in an aluminum pan and subjected to a constant temperature of 144 °C for 40 min. The crosslink density of the vulcanizates was evaluated by the swelling in toluene. The swelling ratio and crosslink density of vulcanizates were calculated according to the Flory–Rehner theory.^{52,53} Values reported represent the averages obtained from three specimens. To investigate the reactivity of ZnO with StH, the compounds were compressed at 144 °C at various time intervals (0, 5, 10, 15, and 30 min). These samples were then analysed using the FT-IR technique (Frontier, PerkinElmer). Tensile properties of vulcanizates were tested according to ISO 37 using a universal testing machine (Model 5566; Instron Co.). The reported tensile stress–strain curve for each sample represents a curve closest to the average obtained from five specimens. Hardness was measured with a Shore A hardness tester in compliance with ISO 7619, and the average value for each specimen was calculated from measurements at ten different positions.

3 Results and discussion

3.1 Characterizations of skim latex serum wastewater

Skim latex serum is the wastewater from the concentrated latex production process. As mentioned earlier, the major



component in the skim latex serum is water. Other components such as proteins, lipids, and carbohydrates/sugars, *e.g.*, L-quebrachitol, sucrose, glucose, fructose, raffinose, and pentose are also found in the skim latex serum.⁴² The FT-IR spectrum of the frozen-dried skim latex serum (Fig. 2a) is shown in Fig. 2b and c, and the peak assignment of its FT-IR spectrum is summarized in Table 1. The absorption bands at 1644 cm^{-1} and 1571 cm^{-1} , assigned to C=O stretching and N-H bending vibrations of the mono-substituted amide, indicated the presence of the proteins in the skim latex serum.⁵⁴ The FT-IR result corresponded well to about $30.8 \pm 0.1\%$ N in the frozen-dried skim latex serum determined by nitrogen analysis based on the Kjeldahl method. Moreover, the absorption bands at 3247 cm^{-1} assigned to $-\text{OH}$ (H-bridge) in the hydrogen bond as well as the bands at 1324 cm^{-1} and 1271 cm^{-1} assigned to the O-H bending possibly suggested the existing sugars in the skim latex serum.⁵⁴ These results corresponded well to the biomolecules present in the skim latex serum previously reported.⁴² Both proteins and sugars in the plant extracts have been documented as the reducing, capping, and stabilizing agents for synthesizing metallic particles.⁴⁶

Furthermore, the bands in the range of $951\text{--}710\text{ cm}^{-1}$ assigned to the C-H bending in alkenes (C=C-H) suggested the remaining rubber parts in the skim latex serum.⁵⁴ In this research, the skim latex serum was separated from the skim latex by the centrifugation method. The low molecular weight of rubber (polysisoprene) in the top layer might have escaped to the layer of skim latex serum (Fig. 1 in the Experimental section).

3.2 Synthesis of ZnO using skim latex serum wastewater and its characterizations

In this article, the skim latex serum was used for the green synthesis of ZnO first. The skim latex serum was added into two types of zinc precursor solutions, which were zinc acetate and zinc nitrate solutions. The reaction was stirred for 2 h at r.t. and kept the solutions overnight. The resulting white powder was obtained after sample drying and calcination. Fig. 3 reveals the FE-SEM images of the powder green synthesized when the zinc acetate and zinc nitrate were used as zinc precursors. At low magnification (Fig. 3a), the powder green synthesized from zinc acetate exhibited the mixed morphologies of flower flake-like structure and the pieces of pressed powder. However, the only

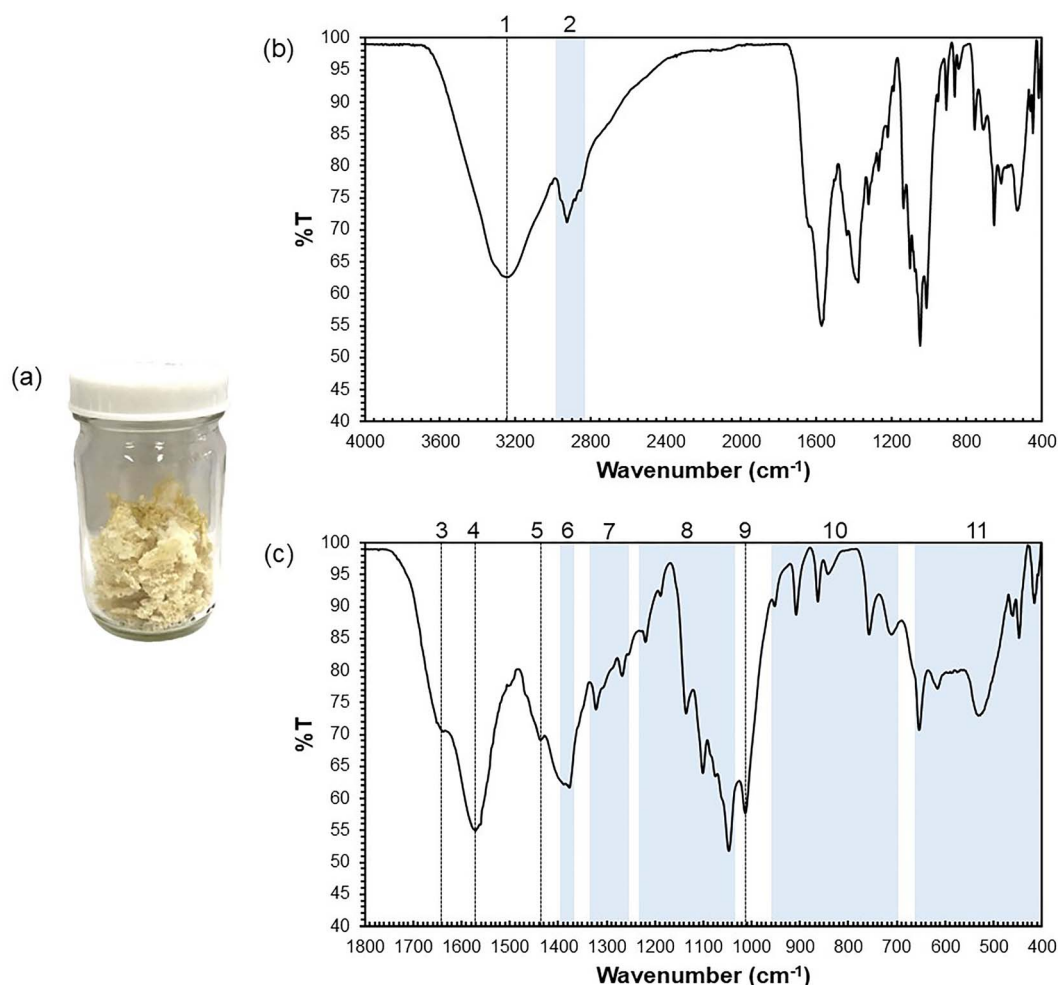


Fig. 2 (a) The frozen-dried skim latex serum and (b) the FT-IR spectrum of the frozen-dried skim latex serum in the range of $4000\text{--}400\text{ cm}^{-1}$ and (c) $1800\text{--}400\text{ cm}^{-1}$.



Table 1 Peak assignment of FT-IR spectrum of the frozen-dried skim latex serum

No.	Wavenumber (cm ⁻¹)	Assignment
1	3247	-OH (H-bridge) in the hydrogen bond
2	2964, 2926, 2883, 2853	C-H stretching in -CH ₃ or -CH ₂
3	1644	C=O stretching in mono-substituted amide (-CO-NH-) or amide I
4	1571	N-H bending in mono-substituted amide (-CO-NH-) or amide II
5	1439	C-H bending in -CH ₃ or -CH ₂
6	1390, 1380	C-H bending in -CH ₃
7	1324, 1271	O-H bending
8	1220, 1190, 1135, 1100, 1049	C-O stretching
9	1011	C-H in primary alcohol/phosphate ions PO ₄ ³⁻
10	951, 909, 862, 841, 759, 710	C=C-H alkenes/aromatic rings
11	652, 615, 530, 460, 448, 415	Alkyl halogen compounds

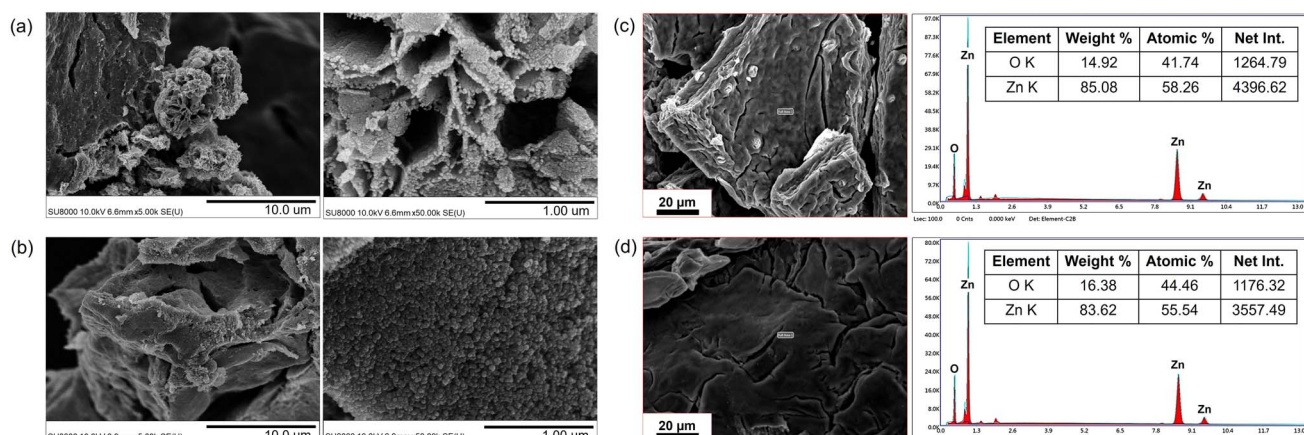


Fig. 3 FE-SEM images of the powder green synthesized from (a) zinc acetate and (b) zinc nitrate. FE-SEM-EDX images of the ZnO powder green synthesized from (c) zinc acetate and (d) zinc nitrate.

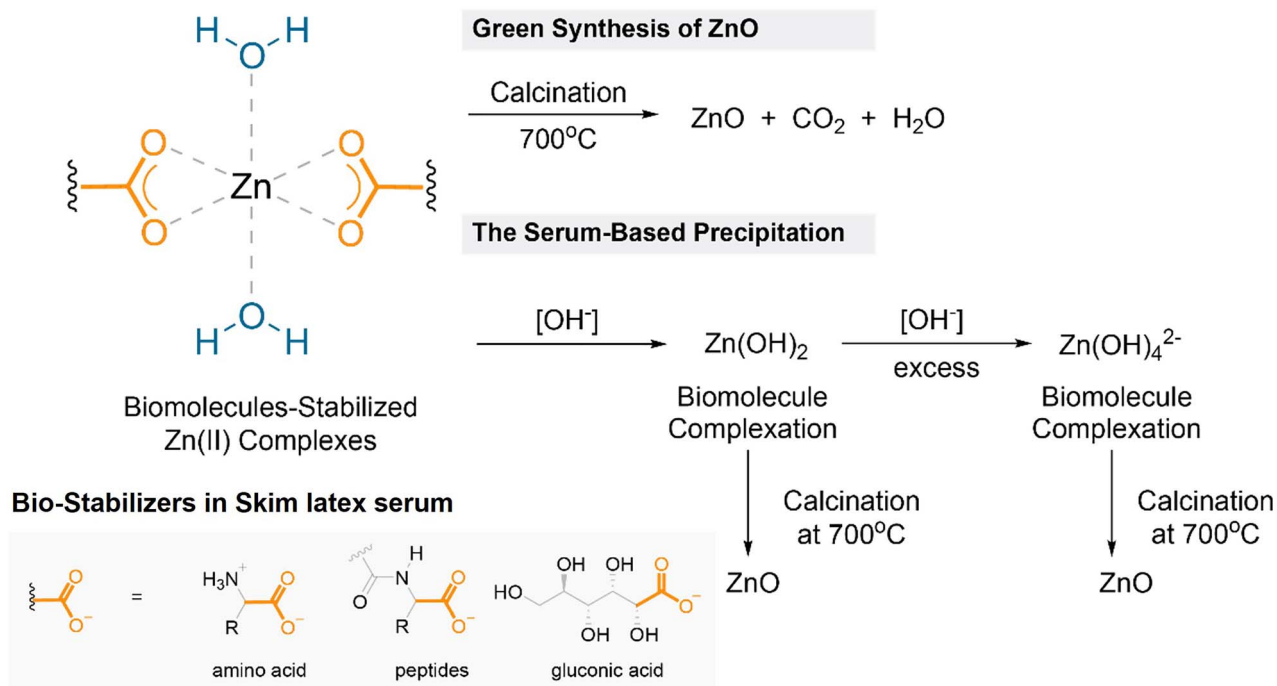
pressed powder morphology was observed in the powder green synthesized from zinc nitrate (Fig. 3b). Their FE-SEM images at higher magnification showed that the assembled structures of both flower flake-like structure and the pieces of pressed powder were made up of the spherically shaped particles with agglomeration, where the average size of the primary particles was about 42.3 ± 9.2 nm and 46.2 ± 13.7 nm in the samples green synthesized from zinc acetate and zinc nitrate, respectively. Fig. 3c and d show the FE-SEM-EDX images of the powder green synthesized using zinc acetate and zinc nitrate as zinc precursors, respectively. It was confirmed that the powder obtained was ZnO. The weight % of the elemental Zn and O for the ZnO green synthesized from zinc acetate was 85% and 15%, and those for the ZnO green synthesized from zinc nitrate were 84% and 16%, respectively.

The possible reaction mechanism for the green synthesis of ZnO is illustrated in Scheme 2. The reaction begins with the coordination of biomolecules within the skim latex serum—such as amino acids, peptides, or gluconic acid (from glucose oxidation)—with Zn(II) precursors through their carboxylate functional groups, leading to the dissociation of Zn(II) ions. Zn(II) ions can further be stabilized with the serum constituents through intermolecular interactions, including hydrogen

bonding and ion-dipole interactions, which help prevent agglomeration and may control particle size. Subsequent calcination at 700 °C in air converts these species into ZnO, producing CO₂ and H₂O as byproducts. According to eqn (1) (Experimental section), the % yields of the green synthesized ZnO from zinc acetate and zinc nitrate were 2% and 3%, respectively. Although the skim latex serum was successfully used as capping and stabilizing agents for the green synthesis of the ZnO, the % yields of the ZnO green synthesized from both zinc precursors were very low. Thus, it brings about the idea of using the skim latex serum with a strong base, NaOH to synthesize the ZnO through the precipitation method.

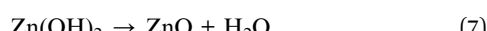
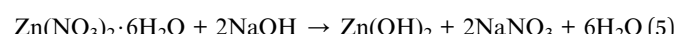
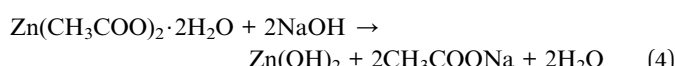
For the serum-based precipitation method, the amounts of skim latex serum added into zinc acetate and zinc nitrate solutions were varied from 0.00, 0.25, 0.50, and 1.00 ml, respectively, while the amount and concentration of the NaOH were kept constant. The ZnO powder of each condition was obtained as shown in Fig. S1. The ZnO powder synthesized from both zinc precursors was pale yellow. However, the ZnO powder synthesized from zinc nitrate (N-ZnO-serum x) had a darker yellow color than that synthesized from zinc acetate (A-ZnO-serum x). When the ZnO is synthesized through the serum-based precipitation method, the ZnO formation may proceed





Scheme 2 The possible reaction mechanisms for ZnO formation through green synthesis and the serum-based precipitation method.

through the alkali precipitation as described in eqn (4) and (5).^{55,56} Initially, the aqueous solution of $\text{Zn}(\text{CH}_3\text{COO})_2 \cdot 2\text{H}_2\text{O}$ or $\text{Zn}(\text{NO}_3)_2 \cdot 6\text{H}_2\text{O}$ reacts with an alkali NaOH solution, yielding zinc hydroxide ($\text{Zn}(\text{OH})_2$), sodium acetate (CH_3COONa) or sodium nitrate (NaNO_3) and water molecules. The zinc hydroxide ($\text{Zn}(\text{OH})_2$) can further react with water molecules, leading to the formation of the zincate anion ($\text{Zn}(\text{OH})_4^{2-}$) (eqn (6)), and subsequently, both $\text{Zn}(\text{OH})_2$ and $\text{Zn}(\text{OH})_4^{2-}$ experience a dehydration reaction, resulting in the formation of ZnO as depicted in eqn (7) and (8).⁵⁵



Another reaction mechanism of ZnO formation through the serum-based precipitation method is illustrated in Scheme 2. The addition of NaOH first generates $\text{Zn}(\text{OH})_2$, and excess NaOH promotes the formation of $\text{Zn}(\text{OH})_4^{2-}$ within the matrix. Both hydroxide species are stabilized by the biomolecules present in the skim latex serum. Upon calcination, those species transform into ZnO. These proposed mechanisms not only advance the understanding of ZnO formation in such unconventional systems but also highlight the unique role of serum constituents in directing precipitation chemistry.

According to eqn (1) (Experimental section), the % yields of the ZnO synthesized by the serum-based precipitation method at all conditions were calculated and reported in Table 2. As expected, the % yields of A-ZnO-serum x and N-ZnO-serum x synthesized by the serum-based precipitation method were significantly higher than those by green synthesis at the same amount of skim latex serum. This is because NaOH increased the concentration of OH^- in the reaction, serving as a source for the formation of $\text{Zn}(\text{OH})_2$ and $\text{Zn}(\text{OH})_4^{2-}$, which subsequently developed into ZnO. This confirms that the presence of these hydroxides appears to facilitate more effective ZnO formation during calcination. Moreover, the yielding of N-ZnO-serum x tended to increase with increasing amounts of skim latex serum. The high solubility and complete dissociation of zinc nitrate ensure a steady supply of Zn(II) ions that readily interact with the skim latex serum. As the amount of serum increased, the biomolecules in the serum facilitated the ZnO formation, resulting in a continuous increase in ZnO yield. A similar trend

Table 2 % Yields of A-ZnO-serum x and N-ZnO-serum x synthesized by the serum-based precipitation method at various amounts of skim latex serum

Amounts of skim latex serum (ml)	% yield	
	A-ZnO-serum x	N-ZnO-serum x
0.00	14%	51%
0.25	46%	68%
0.50	69%	64%
1.00	45%	75%



of yielding was observed for A-ZnO-serum x , up to a skim latex serum amount of 0.50 ml, after which the ZnO yield decreased at a skim latex serum amount of 1.00 ml. In contrast to zinc nitrate, zinc acetate exhibits relatively lower solubility and its acetate ligands can interact competitively with serum constituents. At a lower amount of serum, Zn(II) ions are available for nucleation and ZnO formation. However, at higher amounts of serum, excess biomolecules in the serum and acetate ligands may adsorb onto the ZnO surface or form complexes, thereby reducing the efficiency of ZnO formation. This behavior explains the non-continuous yield trend observed for the ZnO synthesized using zinc acetate, and further indicates that 0.50 ml of skim latex serum represents its optimal synthesis condition. When considering the same amount of skim latex serum used, the % yields of N-ZnO-serum x tended to be higher than those of A-ZnO-serum x . This implied that the use of zinc nitrate in the synthesis of ZnO potentially led to a higher concentration of nuclei or promoted superior growth of ZnO compared to the utilization of zinc acetate, in line with the reason described above.

The A-ZnO-serum x and N-ZnO-serum x at various amounts of skim latex serum were further characterized by FT-IR as shown in Fig. 4a and b. The peak assignment of their FT-IR spectra is summarized in Table 3. The absorption bands of the Zn–O stretching appeared in the range of 600–400 cm^{-1} .^{55,57}

Moreover, the bands at 1330 cm^{-1} and 1325 cm^{-1} observed in the spectra of the A-ZnO-serum x and N-ZnO-serum x , respectively were assigned to the O–H deformation vibration.⁵⁴ This possibly indicated the adsorption of hydroxide on the Zn-polar or O-polar face.⁵⁸ Also, the bands assigned to O–H deformation vibration could be the hydroxyl group of the sugar structure. In addition to the characteristic bands of ZnO, the other bands presenting in the FT-IR spectra of all samples suggested the existing skim latex serum. For example, the bands at 1521 cm^{-1} assigned to N–H bending in mono-substituted amide ($-\text{CO}-\text{NH}-$) or amide II referred to the presence of proteins.⁵⁴ Also, the bands in the range of 981–875 cm^{-1} assigned to the C–H bending in alkenes ($\text{C}=\text{C}-\text{H}$) suggested the remaining rubber parts in the skim latex serum.⁵⁴ For the A-ZnO-serum x , it was clear that the absorption bands assigned to the C–H bending in alkenes became stronger when a higher amount of the skim latex serum was added. As a result, the bands assigned to Zn–O stretching at 570 cm^{-1} and 515 cm^{-1} became broader and disappeared in A-ZnO-serum 0.50 and A-ZnO-serum 1, respectively. This is probably due to the interaction of the rubber part with the synthesized ZnO disturbing the vibration of Zn–O itself. However, this phenomenon was not observed for the N-ZnO-serum x . Based on the FT-IR results, it was confirmed that some of the components in the skim latex serum such as proteins, sugar, and low molecular weight rubber still presented

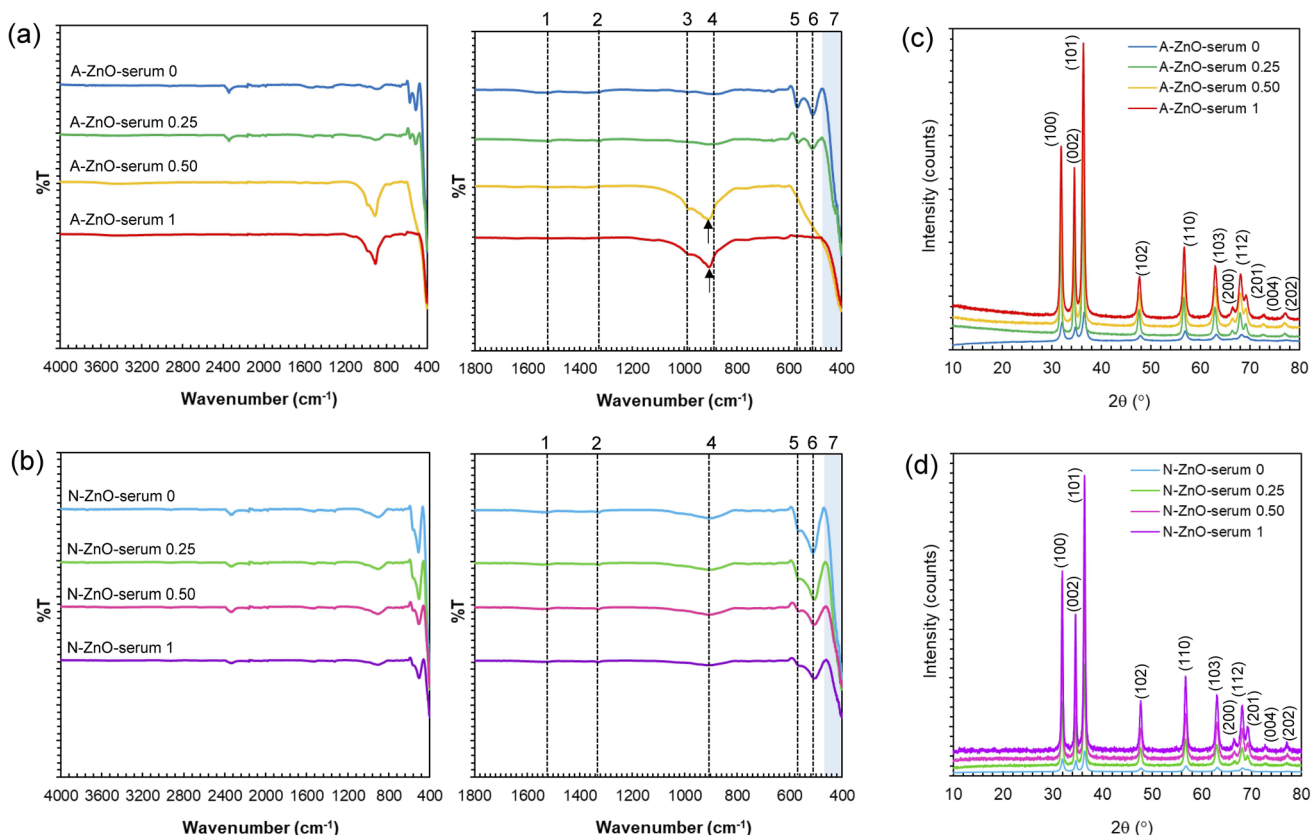


Fig. 4 FT-IR spectra of the (a) A-ZnO-serum x and (b) N-ZnO-serum x synthesized by the serum-based precipitation method at various amounts of skim latex serum. PXRD patterns of (c) A-ZnO-serum x and (d) N-ZnO-serum x synthesized by the serum-based precipitation method at various amounts of skim latex serum.



Table 3 Peak assignment of FT-IR spectra of A-ZnO-serum *x* and N-ZnO-serum *x* synthesized by the serum-based precipitation method at various amounts of skim latex serum

No.	Wavenumber (cm ⁻¹)		Assignment
	A-ZnO-serum <i>x</i>	N-ZnO-serum <i>x</i>	
1	1521	1521	N–H bending in mono-substituted amide (–CO–NH–) or amide II
2	1330	1325	O–H deformation vibration
3	981	—	C=C–H in alkenes
4	875 ^a , 905 ^b	900	C=C–H in alkenes
5	570	570	Zn–O
6	515	510	Zn–O
7	480–400	480–400	Zn–O

^a Observed in A-ZnO-serum 0 and A-ZnO-serum 0.25. ^b Observed in A-ZnO-serum 0.50 and A-ZnO-serum 1.

with the synthesized ZnO although it was dried and calcined at a very high temperature. These results suggested the strong interaction of the skim latex serum and the synthesized ZnO.

The identification of the crystalline structure of the ZnO was confirmed using the PXRD technique. The PXRD patterns of the A-ZnO-serum *x* and N-ZnO-serum *x* at various amounts of skim latex serum are illustrated in Fig. 4c and d, respectively. All the ZnO samples showed the same crystal planes, *i.e.*, (100), (002), (101), (102), (110), (103), (200), (112), (201), (004), and (202). Their diffraction data agreed with JCPDS no. 36-1451, representing the hexagonal wurtzite crystalline structure of ZnO.⁵⁹ The PXRD data exhibited peak patterns exclusively associated with ZnO, indicating the high purity of ZnO derived from both precursors. The sharp and narrow diffraction peaks in their PXRD patterns indicated the excellent crystallinity of the synthesized ZnO. The morphologies of the A-ZnO-serum *x* and N-ZnO-serum *x* at various amounts of skim latex serum were observed by FE-SEM as shown in Fig. 5. Compared to the morphology of the commercial ZnO in hexagonal rod shape in Fig. 5a and f, the ZnO synthesized using both zinc precursors interestingly showed their morphologies in flower-like shape, with several petals developing in a few layers (Fig. 5b–e and g–j). The assembly of the ZnO synthesized from both zinc precursors into a flower-like shape can be seen clearer at higher magnification images.

The possible growth mechanism of flower-like ZnO structure is shown in Fig. 6. In general, the ZnO crystal in the hexagonal wurtzite structure consists of a Zn-polar plane (0001) and an O-polar plane (0001̄), featuring six non-polar faces^{58,60–62} as shown in Fig. 6a. At the initial stage of the reaction, Zn(OH)₄²⁻ ions, identified as growth units near the ZnO particle surface, are likely adsorbed onto the positively charged Zn-polar surface (0001), leading to accelerated growth along the (0001) direction and the formation of hexagonal rod-like ZnO structures (Fig. 6a).^{63–66} However, the growth of ZnO along the (0001) planes can be restricted under certain conditions, such as excessive or abnormal production of the Zn(OH)₄²⁻ growth units relative to the (0001) polar faces (Fig. 6b). In such cases, repulsion of Zn(OH)₄²⁻ on the (0001) plane occurs, and the residual Zn(OH)₄²⁻ subsequently grows on other planes, resulting in the development of flower-like ZnO structures.^{63–66}

The flower-like shape of ZnO observed in A-ZnO-serum 0 and N-ZnO-serum 0 supported the explanation above well. In the absence of skim latex serum, the formation of the flower-like ZnO can be attributed to the high concentration of NaOH applied during the synthesis process.

Additionally, the growth of hexagonal ZnO rod-like structures along the (0001) planes may be constrained by the adsorption of these polar faces by other anions or capping agents (Fig. 6b).^{63–66} In this study, amino acids, peptides, and gluconic acid in the skim latex serum possibly reacted with Zn(II) ions on the positive polar surfaces, forming complexes with zinc. Therefore, the skim latex serum acted as a capping agent layer on the positive polar surfaces of the ZnO structure, causing the reduction in surface energy of the (0001) plane. Thus, the growth rate of ZnO along the (0001) direction became slower. The thickness of the rod-like ZnO increased by steadily decreasing the top part of the rod to form rugby-like ZnO structures (Fig. 6b).⁶⁴ Subsequently, the growth process proceeded in the middle of the rugby-like ZnO structure from the six non-polar facets of a hexagonal wurtzite crystal to form six petals of the flower-shaped ZnO structures. Each petal was half rugby-like and grew in the (0001) direction^{63–66} as shown in Fig. 6b. This was the first proposal for the formation mechanism of flower-like ZnO *via* the serum-based precipitation method. The respective roles of the serum and the alkali (NaOH) in directing this morphology were elucidated.

From the FE-SEM images in Fig. 5g–j, it was evident that the average size of the full array of the flower-like ZnO synthesized using zinc nitrate tended to decrease with increasing amounts of skim latex serum. The size of those ZnO varied from $0.90 \pm 0.16 \mu\text{m}$ to $0.54 \pm 0.13 \mu\text{m}$. This trend can be explained by the role of skim latex serum as capping and stabilizing agents, which influences the balance between nucleation and growth processes. A higher amount of serum provides more biomolecules that promote nucleation and stabilize the formed particles, while simultaneously restricting growth, resulting in smaller ZnO structures. A similar trend was observed for ZnO synthesized using zinc acetate (Fig. 5b–e). The particle size decreased from $0.87 \pm 0.23 \mu\text{m}$ to $0.31 \pm 0.06 \mu\text{m}$ as the skim latex serum increased up to 0.50 ml. However, when the amount of serum reached 1.00 ml, the flower-like ZnO particles became



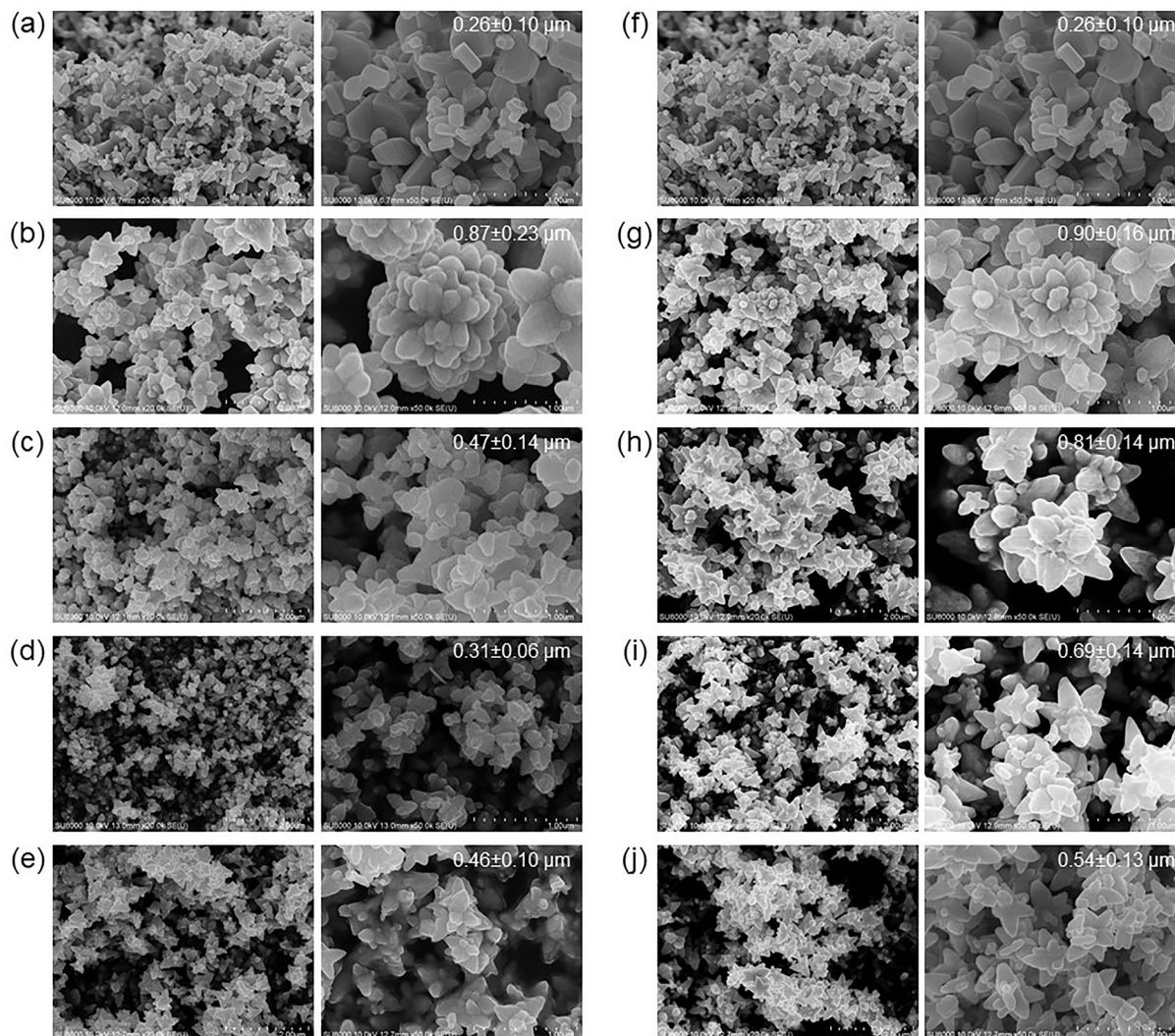


Fig. 5 FE-SEM images of (a and f) commercial ZnO (C-ZnO), (b) A-ZnO-serum 0, (c) A-ZnO-serum 0.25, (d) A-ZnO-serum 0.50, (e) A-ZnO-serum 1, (g) N-ZnO-serum 0, (h) N-ZnO-serum 0.25, (i) N-ZnO-serum 0.50, and (j) N-ZnO-serum 1.

larger ($0.46 \pm 0.10 \mu\text{m}$). This indicates that 0.50 ml of serum may represent an optimal condition for the serum-based precipitation method. Beyond this concentration, an excess of serum could saturate the ZnO surface, thereby reducing the efficiency of further ZnO nucleation and/or promoting particle aggregation. As a result, larger particles are formed and the overall ZnO yield decreases, as also reflected in Table 2. Comparing the same amount of skim latex serum used, the average size of the full array of the flower-like ZnO for A-ZnO-serum x was smaller than that of N-ZnO-serum x . These results suggested that the ZnO synthesized using zinc acetate underwent inferior growth and development into a flower-like shape compared to ZnO synthesized using zinc nitrate. Notably, the multilayers of ZnO petals were less distinctly observed in A-ZnO-serum x than in N-ZnO-serum x . The remaining rubber adsorbed on the A-ZnO-serum 0.50 and A-ZnO-serum 1 as detected in their FT-IR spectra (Fig. 4a) possibly slowed down the growth mechanism of the ZnO

synthesized using zinc acetate. This observation aligned with previous literature, indicating that the size of ZnO synthesized using zinc acetate was smaller than that using zinc nitrate under identical preparation methods.⁶⁷ However, the average size of the full array of the flower-like ZnO synthesized using zinc acetate and zinc nitrate was still bigger than that of the average length of the commercial ZnO (C-ZnO), which was about $0.26 \pm 0.10 \mu\text{m}$.

3.3 Applications of the synthesized ZnO

3.3.1 Photocatalytic dye degradation. In this part, A-ZnO-serum 1 was chosen for investigating the photocatalytic degradation of methylene blue dye due to its smaller particle size compared to N-ZnO-serum 1, with the results subsequently compared to those of C-ZnO, as illustrated in Fig. 7. The degradation efficiency of the dye was studied by recording UV-vis spectra (500–800 nm) of the remaining dye after adding A-ZnO-serum 1 and C-ZnO for various time intervals of 0, 5, 35,



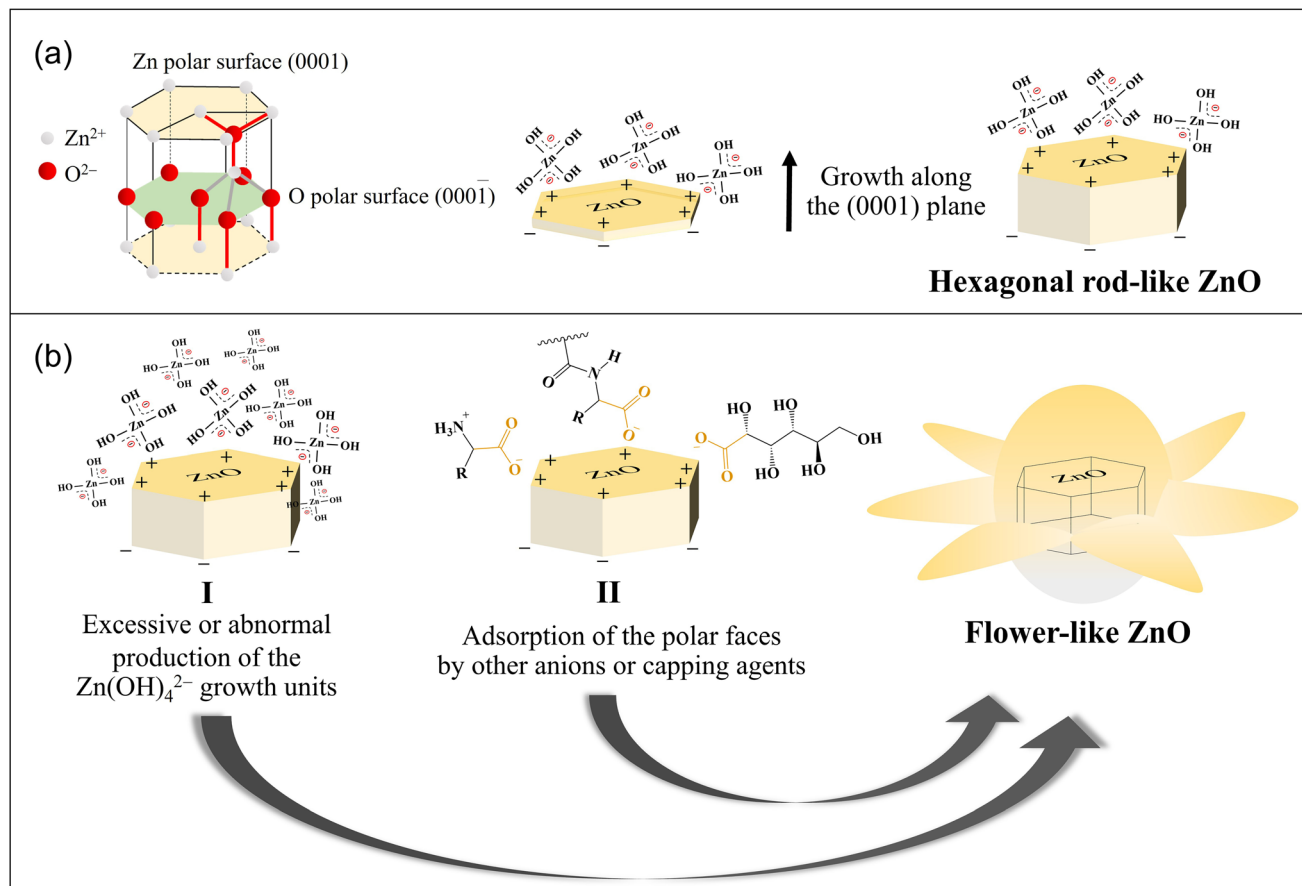


Fig. 6 (a) The possible growth mechanism of hexagonal rod-like ZnO and (b) the possible growth mechanisms of flower-like ZnO synthesized through a serum-based precipitation method.

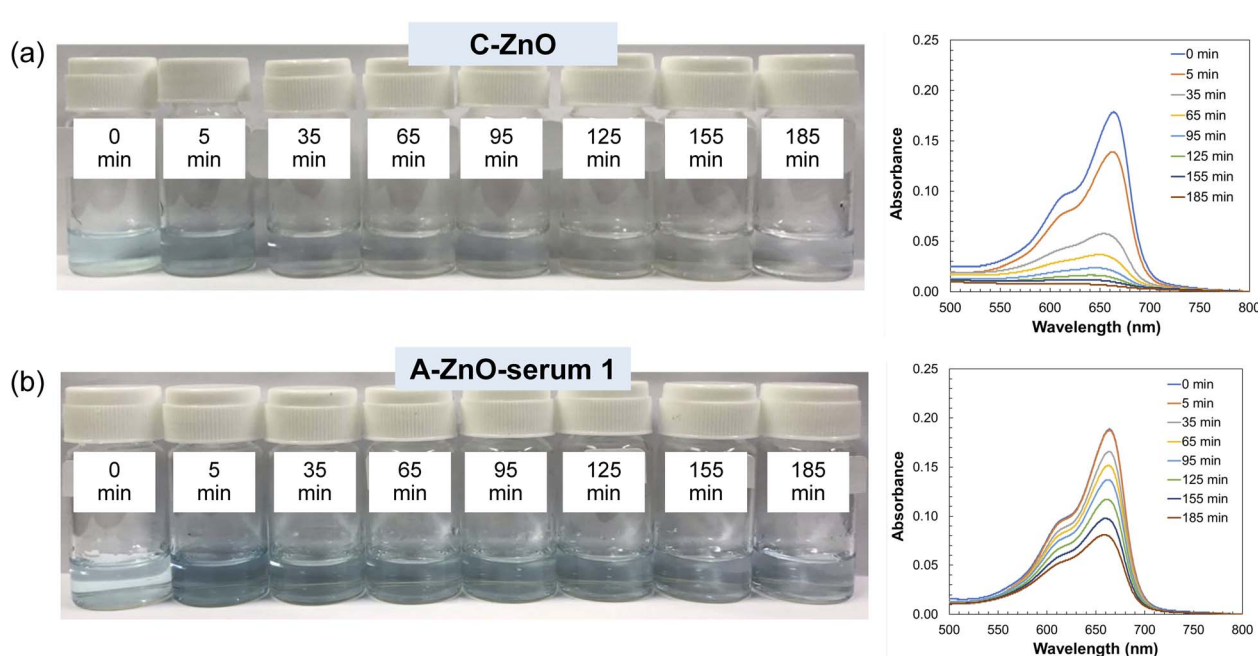


Fig. 7 The photocatalytic degradation of methylene blue dye by (a) C-ZnO and (b) A-ZnO-serum 1 at various UV irradiation durations.

65, 95, 125, 155, and 185 min. The absorption peaks at 614 and 664 nm indicated the existence of the methylene blue dye. The decreasing absorbances at 614 and 664 nm in both samples corresponded well to the change of dye color from dark blue into colorless (Fig. 7). These results suggested that A-ZnO-serum 1 and C-ZnO were able to degrade the methylene blue dye under the UV radiation. Photon-induced electron–hole pairs facilitate reactions on the catalyst's surface, generating superoxide ions and hydroxyl free radicals. These radicals act as potent oxidizing agents, breaking down pollutant chemicals such as methylene blue in wastewater.^{26,68–71} A low concentration of methylene blue (1 ppm) with a relatively high ZnO dosage (1 mg : 1 ml) was used in this study to maximize removal efficiency and clearly evaluate the catalytic performance of the ZnO. This condition also simulated trace-level dye contamination sometimes found in real wastewater streams.

Considering the same time interval, however, the A-ZnO-serum 1 seemed less effective in dye degradation than the C-ZnO. For better comprehension, the time-dependent amount of the dye degraded per unit mass of ZnO is calculated using eqn (2) (Experimental section) and is presented in Fig. 8. It was clear that the amount of dye degraded per unit mass of the A-ZnO-serum 1 was lower than that of the C-ZnO at the same time interval. Interestingly, the behavior of time-dependent dye degradation of the A-ZnO-serum 1 was different from that of the C-ZnO. The amount of dye degraded per unit mass of the A-ZnO-serum 1 tended to gradually increase with a longer time interval, while that of the C-ZnO rapidly increased in the first 40 min, and slightly increased thereafter. To analyze the dye degradation kinetics in more detail, the UV-vis absorption data of both samples were fitted using the pseudo-zero-order, pseudo-first-order, and pseudo-second-order kinetic models according to eqn (9)–(11), respectively.⁷²

$$C_t = -k_0 t + C_0 \quad (9)$$

$$\ln C_t = -k_1 t + \ln C_0 \quad (10)$$

$$1/C_t = k_2 t + 1/C_0 \quad (11)$$

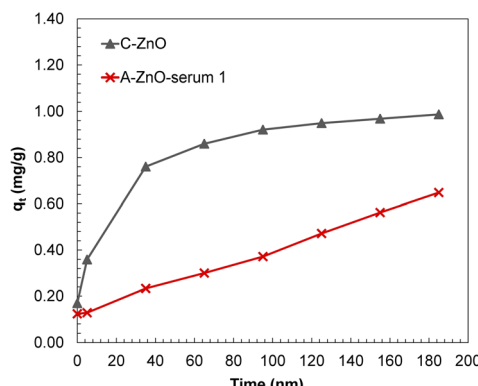


Fig. 8 The time-dependent amount of the dye degraded per unit mass of C-ZnO and A-ZnO-serum 1.

where C_0 and C_t are the concentrations of the methylene blue at 0 and t min, and k_0 , k_1 , and k_2 are the pseudo-zero-order, pseudo-first-order, and pseudo-second-order rate constants, respectively.

The fitted curves of the photocatalytic dye degradation using the C-ZnO and A-ZnO-serum 1 based on the pseudo-zero-order, pseudo-first-order, and pseudo-second-order kinetic models are shown in Fig. S2. Considering the fitting correlation coefficient (R^2) in Table 4, the photocatalytic dye degradation using the C-ZnO exhibited the best fit to the pseudo-first-order kinetic model with R^2 of 0.9761 and the rate constant of 0.017 ppm min⁻¹. In the pseudo-first-order reaction, the reaction rate depends mainly on the concentration of a single reactant, since the concentrations of other reactants are so high and their concentrations do not change significantly during the reaction.^{73,74} This implied that the rate of photocatalytic dye degradation using the C-ZnO in this study possibly depended on the concentration of methylene blue dye because the concentration of ZnO added into the dye solution was much higher than that of methylene blue (1 mg ZnO : 1 ml methylene blue solution). This corresponded well to the time-dependent amount of the dye degraded per unit mass of the C-ZnO in Fig. 8. The increase in the amount of dye degraded was very fast in the early stage of UV irradiation because of the high concentration of methylene blue dye. However, the increase in the amount of dye degraded became slower at longer UV irradiation due to the dilution of the methylene blue dye. Interestingly, the photocatalytic dye degradations using A-ZnO-serum 1 demonstrated the best fit to the pseudo-zero-order kinetic model with an R^2 of 0.9977. The rate constant extracted from the fitted curves of the photocatalytic dye degradations using the A-ZnO-serum 1 was 0.0028 ppm min⁻¹. In general, the rate of a pseudo-zero-order reaction remains constant and is independent of the reactant concentration. Although it may seem counterintuitive for a reaction rate that is independent of reactant concentration, these reactions are frequently observed when all active sites on a catalyst surface, such as ZnO, are saturated with adsorbed species. In the present study, the relatively low concentration of methylene blue dye suggested that the surface of A-ZnO-serum 1 was already extensively covered by residual biomolecules originating from the synthesis process. These residual surface species likely competed with dye molecules for adsorption sites, thereby limiting the availability of active sites and contributing to the observed pseudo-zero-order behavior.^{73,75}

In addition to photodegradation, the recyclability of a photocatalyst is a vital characteristic that determines its practical

Table 4 The fitting correlation coefficient (R^2) and kinetic rate constants of C-ZnO and A-ZnO-serum 1 calculated by fitting with different kinetic models

Samples	Pseudo-zero-order		Pseudo-first-order		Pseudo-second-order	
	R^2	k_0	R^2	k_1	R^2	k_2
C-ZnO	0.7171	0.0038	0.9761	0.017	0.9007	0.1642
A-ZnO-serum 1	0.9977	0.0028	0.9782	0.0045	0.9290	0.0079



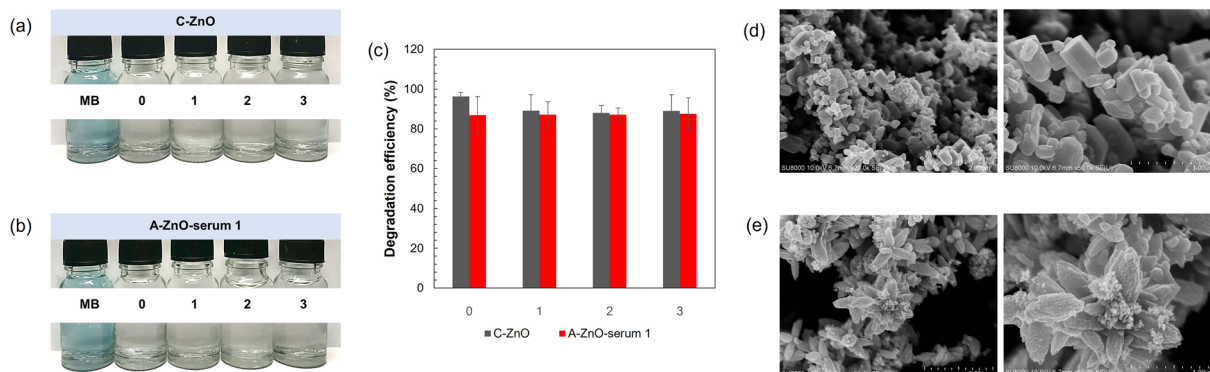


Fig. 9 Recyclability of (a) C-ZnO, (b) A-ZnO-serum 1 for dye degradation, and (c) their corresponding degradation efficiency. FE-SEM images of (d) C-ZnO and (e) A-ZnO-serum 1 after dye degradation test.

use. Fig. 9 presents the recyclability of C-ZnO and A-ZnO-serum 1 for dye degradation. Each ZnO was repeatedly used for three cycles for dye degradation. Although each ZnO was used for three cycles, its efficiency for dye degradation was still high, which was about 89% and 88% for C-ZnO and A-ZnO-serum 1, respectively. As can be seen in the images, the methylene blue dye solutions were very clear after exposure under UV light for 185 min at the last cycle. A closer examination of the recycling performance revealed some differences between the two types of ZnO. The degradation efficiency of C-ZnO showed a slight decline of about 7% after the first cycle, after which it stabilized during the subsequent cycles. In contrast, A-ZnO-serum 1 maintained nearly constant efficiency across all three cycles. The pseudo-first-order kinetics observed in C-ZnO is often associated with physisorption, where dye molecules are bound to the surface through non-covalent interactions such as electrostatic attraction, hydrogen bonding, ion-dipole interaction, and van der Waals forces.⁷⁶ Such interactions allow desorption, enabling recyclability since the ZnO surface remains largely unaltered during repeated use. In contrast, A-ZnO-serum 1

exhibited pseudo-zero-order kinetics, indicating that the reaction rate was limited by surface site saturation.⁷⁶ This behavior can be attributed to residual biomolecules from the synthesis process that remain bound to the ZnO surface even after calcination, occupying part of the active sites through chemisorption. Meanwhile, dye molecules likely adsorb mainly *via* physisorption, allowing them to be removed after each cycle and leaving the ZnO surface available for reuse. The stable degradation efficiency of A-ZnO-serum 1 across three cycles was further supported by its larger BET surface area ($18.45 \pm 0.05 \text{ m}^2 \text{ g}^{-1}$) compared with that of C-ZnO ($4.51 \pm 0.04 \text{ m}^2 \text{ g}^{-1}$). Its abundant surface sites likely remain physically adsorbed and effectively regenerated after each cycle, rather than being irreversibly blocked. However, residual biomolecules on A-ZnO-serum 1 may limit dye adsorption, which could explain the comparable overall efficiencies observed between the two types of ZnO. Furthermore, the FE-SEM images in Fig. 9 suggested that the morphologies of the C-ZnO and A-ZnO-serum 1 after the dye degradation test were unchanged. The hexagonal rod-like shape morphology was observed for the C-ZnO. Also, the

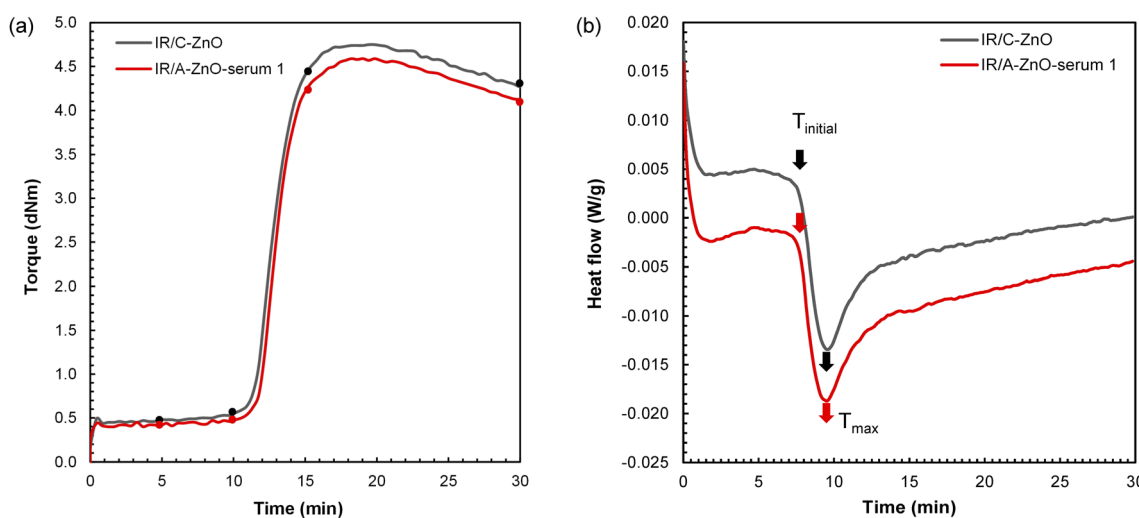


Fig. 10 (a) Cure curves and (b) DSC curves of the IR/C-ZnO and IR/A-ZnO-serum 1 at a constant temperature of 144 °C.



Table 5 Cure properties of the IR/C-ZnO and the IR/A-ZnO-serum 1

Sample	T_{s2} (min)	T_{c90} (min)	Cure rate index	$M_H - M_L$ (dN M)	Swelling ratio	Cross-link density ($\times 10^{-5}$ mol cm $^{-3}$)
IR/C-ZnO	12.63 ± 0.05	14.79 ± 0.03	46.37 ± 0.05	4.29 ± 0.05	4.82 ± 0.06	3.226 ± 0.064
IR/A-ZnO-serum 1	12.86 ± 0.06	15.03 ± 0.33	46.74 ± 6.05	4.19 ± 0.01	4.97 ± 0.01	3.017 ± 0.008

A-ZnO-serum 1 still exhibited the flower-like shape morphology. This suggested the robustness and stability of these ZnO structures under the conditions of the dye degradation test.

3.3.2 Activator for rubber vulcanization. ZnO is a critical rubber-compounding agent in sulfur-based rubber vulcanization. It functions primarily as an activator, activating the vulcanization process by enhancing the efficiency of accelerators in the crosslinking reaction. In this study, the A-ZnO-serum 1 was incorporated into synthetic IR along with other curing agents to prepare the IR vulcanizate. The curing behaviors and mechanical properties of the resulting IR/A-ZnO-serum 1 vulcanizate were subsequently investigated and compared to those of a reference IR vulcanizate prepared using commercial ZnO (IR/C-ZnO). Fig. 10a shows the cure curves of the IR/A-ZnO-serum 1 and IR/C-ZnO, as obtained from the MDR measurement at 144 °C. The corresponding cure properties, namely scorch time (T_{s2}), cure time (T_{c90}), cure rate index, torque difference ($M_H - M_L$), swelling ratio, and the cross-link density are summarized in Table 5. The values of T_{s2} , T_{c90} , and the cure rate index of IR/A-ZnO-serum 1 were found to be closely comparable to those of IR/C-ZnO, suggesting similar overall curing kinetics. However, the $M_H - M_L$ of IR/A-ZnO-serum 1 was slightly lower than that of IR/C-ZnO, which corresponded to its marginally higher swelling ratio and reduced cross-link density. These may be attributed to the relatively larger assembled flower-like structure of A-ZnO-serum 1 and less uniform morphology, in comparison to C-ZnO.^{77,78}

Fig. 10b displays the DSC curves of IR/A-ZnO-serum 1 and IR/C-ZnO. Both samples exhibited the exothermic peaks, indicating the presence of vulcanization reaction in IR compounds. The initial vulcanization time (t_{init}) and complete vulcanization time (t_{max}) of both IR compounds were determined from the DSC curves. The values for t_{init} and t_{max} of A-ZnO-serum 1 were found to be 7.63 and 9.48 min, respectively, while those of C-ZnO were 7.74 and 9.53 min, respectively. These findings confirm that A-ZnO-serum 1 effectively functions as an activator in the vulcanization of rubber, comparable in performance to C-ZnO.

In rubber compounding, ZnO is commonly incorporated together with stearic acid, which serves as a co-activator in sulfur vulcanization. The synergistic action of ZnO and stearic acid provides significantly greater activation of the vulcanization process compared to the use of ZnO alone. Here, the reactivity of ZnO with stearic and other curing agents during the vulcanization of IR was examined through detailed FT-IR spectral analysis. IR compounds were subjected to compression molding at 144 °C for varying durations corresponding to specific time points (5, 10, 15, and 30 min), as marked by dots on the cure curves in Fig. 10a. Following compression at each designated time interval, the samples were collected and analyzed using FT-IR spectroscopy.

The resulting spectra are presented in Fig. 11. To further examine the coordination between ZnO and stearic acid in IR compounds, the FT-IR spectra were specifically analyzed in the range of 1620–1520 cm $^{-1}$. Within this range, the absorption bands at approximately 1540 and 1595 cm $^{-1}$, corresponding to the asymmetric stretching of monodentate and *syn-syn* bridging bidentate coordinations of zinc-carboxylate complex, respectively (Fig. 11), were clearer observed. Notably, these characteristic bands appeared more prominently in the FT-IR spectrum of IR/A-ZnO-serum 1 at 0 minutes of heating, compared to that of IR/C-ZnO (Fig. 11). The results suggested that the reaction between the A-ZnO-serum 1 could react with stearic acid since r.t. during mixing. Upon heating for 5 min, the intensities of both bands increased in IR/A-

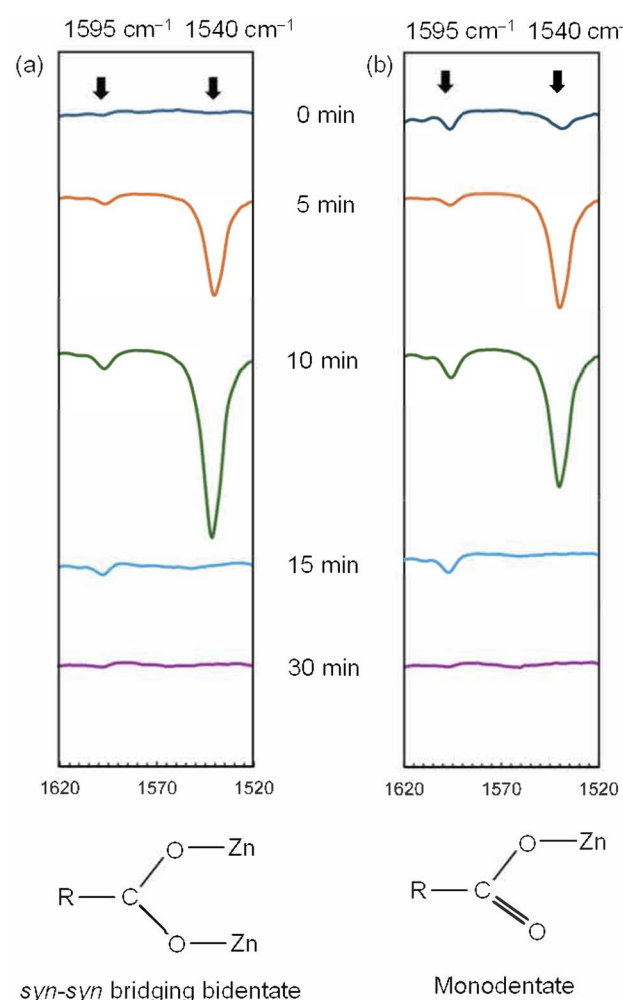


Fig. 11 FT-IR spectra of (a) IR/C-ZnO and (b) IR/A-ZnO-serum 1 in the range of 1620–1520 cm $^{-1}$.



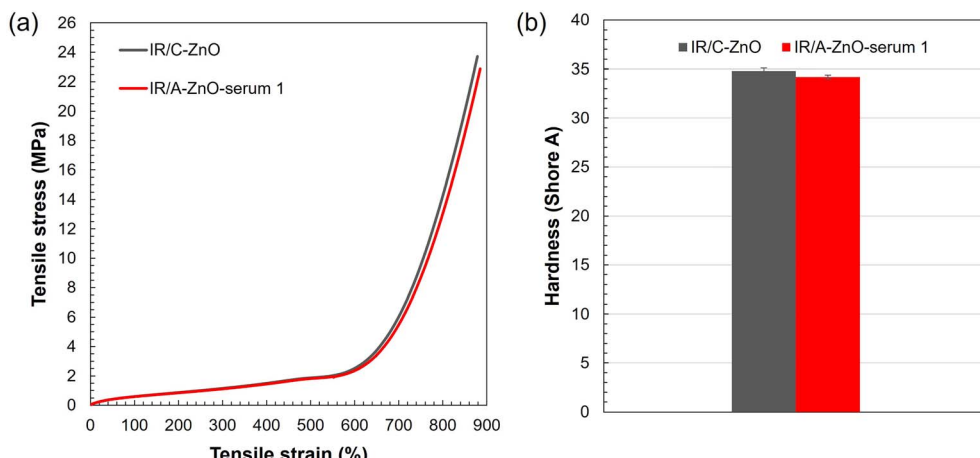


Fig. 12 (a) Tensile properties and (b) hardness (Shore A) of IR/C-ZnO and IR/A-ZnO-serum 1.

ZnO-serum 1 and IR/C-ZnO samples. Notably, the band at 1540 cm^{-1} became predominant, indicating the enhanced formation of monodentate coordination between zinc ions and stearate ligands.⁷⁹ However, after 10 min of heating—relating to the point immediately following the major torque increase on the cure curve, where the onset of three-dimensional cross-linking is likely to occur—these bands began to diminish in intensity or disappear. This observation may suggest the dissociation of the zinc-stearate complexes, facilitating subsequent reactions between the released zinc species and other vulcanizing agents in the later stages of the curing process. Overall, the results confirm that A-ZnO-serum 1 functions effectively as a vulcanization activator and exhibits a favorable interaction with stearic acid. Furthermore, the comparable curing behaviour and cross-link densities of both IR/A-ZnO-serum 1 and IR/C-ZnO led to the similar tensile properties and the hardness in the corresponding vulcanizates, as illustrated in Fig. 12. The average tensile strength and strain at break of IR/A-ZnO-serum 1 were about $22.7 \pm 1.1\text{ MPa}$ and $883.2 \pm 10.2\%$, respectively, while those of IR/C-ZnO were about $23.3 \pm 1.6\text{ MPa}$ and $876.1 \pm 12.7\%$, respectively. The average hardness of IR/A-ZnO-serum 1 was *ca.* 34.2 ± 0.2 Shore A, compared with 34.8 ± 0.3 Shore A for IR/C-ZnO.

4 Conclusion

In this study, the skim latex serum demonstrated its effectiveness in the sustainable synthesis of ZnO. The biomolecules such as amino acids, peptides, and gluconic acid in the serum acted as the capping and stabilizing agents for ZnO synthesis. Through the serum-based precipitation method, the yielding of ZnO synthesized was remarkably twenty-five times increased, compared to the green synthesis method. Interestingly, the morphology of the synthesized ZnO by the serum-based precipitation method exhibited a distinctive flower-like shape. The size of the flower-like ZnO could be controlled by adjusting the amount of the serum added to the reaction. The serum seemed to promote the nucleation process by stabilizing the resulting ZnO nuclei, relating to the increase in ZnO yield. However, the adsorption of the serum

on the Zn polar surface seemed to decelerate the growth of ZnO on that Zn polar plane, causing the smaller size of flower-like ZnO. Flower-like ZnO functioned effectively as a photocatalyst for dye degradation, following the pseudo-zero-order kinetics. It showed good recyclability, retaining about 88% efficiency after three cycles. Furthermore, the flower-like ZnO served as an activator for the rubber vulcanization reaction. It exhibited favourable interactions with co-activator stearic acid, primarily through monodentate coordination during vulcanization. The curing behaviour and mechanical properties of the rubber vulcanizates using the flower-like ZnO were closely comparable to those of the rubber vulcanizates using commercial ZnO.

Overall, this work is the first to propose a reaction mechanism for ZnO synthesis from skim latex serum wastewater, identifying plausible pathways *via* the serum-based precipitation method. It is also the first to explain the formation of flower-like ZnO in this system, clarifying the roles of serum constituents and NaOH in controlling morphology. The use of skim latex serum wastewater not only converts an industrial by-product into a high-value material but also demonstrates dual applicability in environmental remediation and rubber technology. A key challenge that remains is further increasing the batch yield of ZnO to support industrial scale-up. Future studies will focus on optimizing synthesis conditions, identifying factors influencing ZnO yield, and evaluating the role of individual serum components through model experiments. This research contributes to the advancement of sustainable industrial practices by integrating waste valorization with functional material development and offering a viable alternative to commercial ZnO.

Author contributions

S. N. wrote the original draft, conducted the review and editing, prepared visualizations, curated data, performed formal analysis, carried out investigations, and developed the methodology for this article. T. B. conducted the review and editing, provided resources, and supported research funding. P. J. supervised the project, wrote the original draft, conducted the review and



editing, provided resources, prepared visualizations, performed formal analysis, carried out investigations, and developed the methodology for this article.

Conflicts of interest

There are no conflicts to declare.

Data availability

All relevant data are included in the paper or its supplementary information (SI). Supplementary information: the photos of ZnO powder synthesized by the serum-based precipitation method using zinc acetate and zinc nitrate as zinc precursors with various amounts of skim latex serum. Kinetic study of photocatalytic degradation of methylene blue using commercial ZnO (C-ZnO) and A-ZnO-serum 1. See DOI: <https://doi.org/10.1039/d5ra06278k>.

Acknowledgements

This research project has been supported by Mahidol University (Fundamental Fund: fiscal year 2025 by National Science Research and Innovation Fund (NSRF), Grant Number FF-077/2568). The authors thank Kokoku Intech Co., Ltd for providing the isoprene rubber, and extend our thanks to Mahidol University-Frontier Research Facility (MU-FRF) and scientists of MU-FRF, Nawapol Udpuay, Dr Suwilai Chaveanghong, and Bancha Panyacharoen for instrumentation support for the powder X-ray diffractometer (PXRD, Bruker, D2 Phaser) and their kind assistance. The authors would like to thank Prof. Pranee Phinyocheep for her advice. Also, the authors extend our thanks to Dr Adul Nampaiboon, Ms Kattareen Boonchuay, and Mr Prin Tumwised, the staff of the Rubber Technology Research Centre, Mahidol University, Thailand for their experimental support.

References

- 1 D. Parajuli, D. Kc, K. B. Khattri, D. R. Adhikari, R. A. Gaib and D. K. Shah, *Sci. Rep.*, 2023, **13**, 12193.
- 2 Y. Wang, C. Wang, Y. Xu and Y. Sun, *Mater. Res. Bull.*, 2023, **168**, 112451.
- 3 M. Aliannezhadi, S. Z. Mirsanaee, M. Jamali and F. Shariatmadar Tehrani, *Sci. Rep.*, 2024, **14**, 2035.
- 4 S. Pandey, A. Srivastava, P. Rawat, S. K. Chauhan, A. Ram, V. K. Diwedi, R. K. Shukla and N. Wadhwani, *ACS Omega*, 2024, **9**, 45169–45189.
- 5 S. Pandey, P. Rawat, A. Ram, S. K. Chauhan, R. N. Singh, R. K. Shukla and A. Srivastava, *J. Mol. Struct.*, 2024, **1317**, 139068.
- 6 V. Marunganathan, M. S. K. Kumar, Z. A. Kari, J. Giri, M. R. Shaik, B. Shaik and A. Guru, *Mol. Biol. Rep.*, 2024, **51**, 89.
- 7 P. Perumal, N. A. Sathakkathulla, K. Kumaran, R. Ravikumar, J. J. Selvaraj, V. Nagendran, M. Gurusamy, N. Shaik, S. Gnanavadivel Prabhakaran, V. Suruli Palanichamy, V. Ganesan, P. P. Thiraviam, S. Gunalan and S. Rathinasamy, *Sci. Rep.*, 2024, **14**, 2204.
- 8 A. Shoaib, S. Shahid, S. Mansoor, M. Javed, S. Iqbal, S. Mahmood, A. Bahadur, F. Jaber and M. Alshalwi, *Sci. Rep.*, 2024, **14**, 2499.
- 9 V. Jaiswal, M. Samant, A. Kadir, K. Chaturvedi, A. B. Nawale, V. L. Mathe and P. M. Dongre, *J. Inorg. Organomet. Polym. Mater.*, 2017, **27**, 1211–1219.
- 10 X. Qin, H. Xu, G. Zhang, J. Wang, Z. Wang, Y. Zhao, Z. Wang, T. Tan, M. R. Bockstaller, L. Zhang and K. Matyjaszewski, *ACS Appl. Mater. Interfaces*, 2020, **12**, 48007–48015.
- 11 Z. Liu, S. Xing, Y. Li, J. Sun, H. Li, X. Gu and S. Zhang, *J. Colloid Interface Sci.*, 2024, **661**, 307–316.
- 12 R. Y. Ghareeb, E. B. Belal, N. M. M. El-Khateeb and B. A. Shreef, *BMC Plant Biol.*, 2024, **24**, 110.
- 13 X. Chen, Z. Wu, D. Liu and Z. Gao, *Nanoscale Res. Lett.*, 2017, **12**, 143.
- 14 K. Sakata, K. Minhová Macounová, R. Nebel and P. Krtík, *SN Appl. Sci.*, 2020, **2**, 203.
- 15 A. S. Lanje, S. J. Sharma, R. S. Ningthoujam, J. S. Ahn and R. B. Pode, *Adv. Powder Technol.*, 2013, **24**, 331–335.
- 16 G. Applerot, A. Lipovsky, R. Dror, N. Perkas, Y. Nitzan, R. Lubart and A. Gedanken, *Adv. Funct. Mater.*, 2009, **19**, 842–852.
- 17 Z. R. Dai, Z. W. Pan and Z. L. Wang, *Adv. Funct. Mater.*, 2003, **13**, 9–24.
- 18 A. Król, P. Pomastowski, K. Rafińska, V. Railean-Plugaru and B. Buszewski, *Adv. Colloid Interface Sci.*, 2017, **249**, 37–52.
- 19 H. Agarwal, S. Venkat Kumar and S. Rajeshkumar, *Resour.-Effic. Technol.*, 2017, **3**, 406–413.
- 20 J. Singh, T. Dutta, K.-H. Kim, M. Rawat, P. Samddar and P. Kumar, *J. Nanobiotechnol.*, 2018, **16**, 84.
- 21 R. P. Singh, V. K. Shukla, R. S. Yadav, P. K. Sharma, P. K. Singh and A. C. Pandey, *Adv. Mater. Lett.*, 2011, **2**, 313–317.
- 22 M. R. Anilkumar, H. P. Nagaswarupa, K. S. Anantharaju, K. Gurushantha, C. Pratapkumar, S. C. Prashantha, T. R. Shashi Shekhar, H. Nagabhushana, S. C. Sharma, Y. S. Vidya and D. Prasad, *Mater. Res. Express*, 2015, **2**, 035011.
- 23 M. S. Geetha, H. Nagabhushana and H. N. Shivananjaiah, *J. Sci.:Adv. Mater. Devices*, 2016, **1**, 301–310.
- 24 S. C. Sharma, *Optik*, 2016, **127**, 6498–6512.
- 25 K. K. Panda, D. Golari, A. Venugopal, V. M. M. Achary, G. Phaomei, N. L. Parinandi, H. K. Sahu and B. B. Panda, *Antioxidants*, 2017, **6**, 35.
- 26 K. H. Sudheer Kumar, N. Dhananjaya and L. S. R. Yadav, *J. Sci.:Adv. Mater. Devices*, 2018, **3**, 303–309.
- 27 F. Ameen, T. Dawoud and S. AlNadhari, *Environ. Res.*, 2021, **202**, 111700.
- 28 M. Golmohammadi, M. N. Hassankiadeh and L. Zhang, *Ceram. Int.*, 2021, **47**, 29303–29308.
- 29 M. Hasan, M. Altaf, A. Zafar, S. G. Hassan, Z. Ali, G. Mustafa, T. Munawar, M. S. Saif, T. Tariq, F. Iqbal, M. W. Khan, A. Mahmood, N. Mahmood and X. Shu, *Mater. Sci. Eng., C*, 2021, **119**, 111280.
- 30 J. Li, Y. Li, H. Wu, S. Naraginti and Y. Wu, *Environ. Res.*, 2021, **200**, 111433.



31 H. Sadiq, F. Sher, S. Sehar, E. C. Lima, S. Zhang, H. M. N. Iqbal, F. Zafar and M. Nuhanović, *J. Mol. Liq.*, 2021, **335**, 116567.

32 G. Yashni, A. Al-Gheethi, R. M. S. Radin Mohamed, N. V. Dai-Viet, A. A. Al-Kahtani, M. Al-Sahari, N. J. Nor Hazhar, E. Noman and S. Alkhadher, *Chemosphere*, 2021, **281**, 130661.

33 E. Yoki Yulizar, D. O. B. Apriandanus and R. Marcony Surya, *Ceram. Int.*, 2022, **48**, 3564–3577.

34 T. Gur, I. Meydan, H. Seckin, M. Bekmezci and F. Sen, *Environ. Res.*, 2022, **204**, 111897.

35 V. Dhiman, N. Kondal and P. Choudhary, *Environ. Res.*, 2023, **216**, 114751.

36 U. Manojkumar, D. Kaliannan, V. Srinivasan, B. Balasubramanian, H. Kamyab, Z. H. Mussa, J. Palaniyappan, M. Mesbah, S. Chelliapan and S. Palaninaicker, *Chemosphere*, 2023, **323**, 138263.

37 R. S. Matos, J. M. Attah-Baah, M. D. S. Monteiro, B. F. O. Costa, M. A. Mâcedo, R. S. Silva Junior, H. D. da Fonseca Filho, R. M. P. B. Oliveira and N. S. Ferreira, *J. Mater. Res. Technol.*, 2023, **22**, 2673–2689.

38 P. Maijan, T. Waen-ngoen, S. Suwanboon, S. Chantarak and S. P. Voravuthikunchai, *Inorg. Chem. Commun.*, 2024, **162**, 112086.

39 A. Sowińska-Baranowska and M. Maciejewska, *Int. J. Mol. Sci.*, 2025, **26**, 1101.

40 M. Alvand Ghiasvand, S. Sedaghat, M. R. Allah Gholi Ghasri, F. Motiei and F. R. Nikmaram, *Int. J. New Chem.*, 2025, **12**, 754–773.

41 E. E. Elemike, F. C. Ibeh, W. Iwwurie and D. C. Onwudiwe, *Chem. Pap.*, 2023, **77**, 7717–7724.

42 V. Mardina and F. Yusof, in *Multifaceted Protocol in Biotechnology*, ed. A. Amid, S. Sulaiman, D. N. Jimat and N. F. M. Azmin, Springer Singapore, Singapore, 2018, pp. 179–196, DOI: [10.1007/978-981-13-2257-0_15](https://doi.org/10.1007/978-981-13-2257-0_15).

43 J. T. Tadeusz Haponiuk, J. Kucińska-Lipka, J. Rafal Kędzia and A. Maria Sitko, in *Application and Characterization of Rubber Materials*, ed. G. Akin Evingür and Ö. Pekcan, IntechOpen, Rijeka, 2022, DOI: [10.5772/intechopen.107985](https://doi.org/10.5772/intechopen.107985).

44 Ministry of Natural Resources and Environment, Pollution Control Department, *Best Practices for the Prevention and Reduction of Pollution from the Concentrated Latex*, Bangkok, Thailand, 2005.

45 T. Jullabuth and P. Danwanichakul, *Engineering and Applied Science Research*, 2021, **48**, 422–431.

46 A. K. Sidhu, N. Verma and P. Kaushal, *Frontiers in Nanotechnology*, 2022, **3**, 801620.

47 R. M. Thankachan, N. Joy, J. Abraham, N. Kalarikkal, S. Thomas and O. S. Oluwafemi, *Mater. Res. Bull.*, 2017, **85**, 131–139.

48 S. Bhatia and N. Verma, *Mater. Res. Bull.*, 2017, **95**, 468–476.

49 C. A. Soto-Robles, P. A. Luque, C. M. Gómez-Gutiérrez, O. Nava, A. R. Vilchis-Nestor, E. Lugo-Medina, R. Ranjithkumar and A. Castro-Beltrán, *Results Phys.*, 2019, **15**, 102807.

50 R. Rathnasamy, P. Thangasamy, R. Thangamuthu, S. Sampath and V. Alagan, *J. Mater. Sci.: Mater. Electron.*, 2017, **28**, 10374–10381.

51 O. A. Oyewo, A. Adeniyi, B. B. Sithole and M. S. Onyango, *ACS Omega*, 2020, **5**, 18798–18807.

52 S. Rabiei and A. Shojaei, *Eur. Polym. J.*, 2016, **81**, 98–113.

53 L. Wang, M. Du, G. Shan, Z. Wu, Y. Song and Q. Zheng, *Nano Sel.*, 2022, **3**, 965–976.

54 R. Dunmur and M. Murray, *Spectroscopic Methods in Organic Chemistry*, Georg Thieme Verlag KG, Stuttgart, 2nd edn, 2008.

55 S. S. Alias, A. B. Ismail and A. A. Mohamad, *J. Alloys Compd.*, 2010, **499**, 231–237.

56 M. G. Kotresh, M. K. Patil and S. R. Inamdar, *Optik*, 2021, **243**, 167506.

57 K. Swaroop and H. Somashekharappa, *Res. J. Recent Sci.*, 2015, **2277**, 2502.

58 M. W. Allen, D. Y. Zemlyanov, G. I. N. Waterhouse, J. B. Metson, T. D. Veal, C. F. McConville and S. M. Durbin, *Appl. Phys. Lett.*, 2011, **98**, 101906.

59 A. Mendes, C. Granadeiro, A. Leite, E. Pereira, P. Teixeira and F. Pocas, *Nanomaterials*, 2024, **14**, 638.

60 C. Tang, M. J. S. Spencer and A. S. Barnard, *Phys. Chem. Chem. Phys.*, 2014, **16**, 22139–22144.

61 K.-L. Ching, G. Li, Y.-L. Ho and H.-S. Kwok, *CrystEngComm*, 2016, **18**, 779–786.

62 D. Mora-Fonz, T. Lazauskas, M. R. Farrow, C. R. A. Catlow, S. M. Woodley and A. A. Sokol, *Chem. Mater.*, 2017, **29**, 5306–5320.

63 Q. Yu, C. Yu, W. Fu, M. Yuan, J. Guo, M. Li, S. Liu, G. Zou and H. Yang, *J. Phys. Chem. C*, 2009, **113**, 12016–12021.

64 R. Al-Gaashani, S. Radiman, A. R. Daud, N. Tabet and Y. Al-Douri, *Ceram. Int.*, 2013, **39**, 2283–2292.

65 Q. Hu, G. Tong, W. Wu, F. Liu, H. Qian and D. Hong, *CrystEngComm*, 2013, **15**, 1314–1323.

66 C. Rajkumar and R. K. Srivastava, *Opt. Mater.*, 2020, **109**, 110367.

67 M.-A. Gatou, N. Lagopati, I.-A. Vagena, M. Gazouli and E. A. Pavlatou, *Nanomaterials*, 2023, **13**, 122.

68 S. Suganya and S. Vivekanandhan, *J. Aust. Ceram. Soc.*, 2019, **55**, 433–442.

69 F. A. Alharthi, A. A. Alghamdi, A. A. Alothman, Z. M. Almarhoon, M. F. Alsulaiman and N. Al-Zaqri, *Crystals*, 2020, **10**, 441.

70 A. Muthuvel, M. Jothibas and C. Manoharan, *J. Environ. Chem. Eng.*, 2020, **8**, 103705.

71 S. Rahaiee, M. Ranjbar, H. Azizi, M. Govahi and M. Zare, *Appl. Organomet. Chem.*, 2020, **34**, e5705.

72 T. Ratvijitvech, *Polymers*, 2022, **14**, 2749.

73 D. F. Ollis, *Front. Chem.*, 2018, **6**, 378.

74 D. Ollis, *Catal. Today*, 2020, **340**, 7–11.

75 X. Li, S. Anwer, Q. Guan, B. Li, V. Chan, G. Palmisano and L. Zheng, *Chem. Eng. Sci.*, 2024, **284**, 119501.

76 S. S. Ray, R. Gusain and N. Kumar, in *Carbon Nanomaterial-Based Adsorbents for Water Purification*, ed. S. S. Ray, R. Gusain and N. Kumar, Elsevier, 2020, pp. 37–66, DOI: [10.1016/B978-0-12-821959-1.00003-9](https://doi.org/10.1016/B978-0-12-821959-1.00003-9).

77 S. Sahoo and A. K. Bhowmick, *J. Appl. Polym. Sci.*, 2007, **106**, 3077–3083.

78 H. K. Abgorg and S. O. Movahed, *Plast., Rubber Compos.*, 2024, **53**, 168–177.

79 V. Zeleňák, Z. Vargová and K. Györyová, *Spectrochim. Acta, Part A*, 2007, **66**, 262–272.

